
ENTROPY-CONSERVATIVE HIGH-ORDER METHODS FOR HIGH-ENTHALPY GAS FLOWS

Georgii Oblapenko*, Manuel Torrilhon

Chair of Applied and Computational Mathematics, RWTH Aachen,
Schinkelstrasse 52, 52062 Aachen, Germany

*Corresponding author. E-mail: oblapenko@acom.rwth-aachen.de

ABSTRACT

A framework for numerical evaluation of entropy-conservative volume fluxes in gas flows with internal energies is developed, for use with high-order discretization methods. The novelty of the approach lies in the ability to use arbitrary expressions for the internal degrees of freedom of the constituent gas species. The developed approach is implemented in an open-source discontinuous Galerkin code for solving hyperbolic equations. Numerical simulations are carried out for several model 2-D flows and the results are compared to those obtained with the finite volume-based solver DLR TAU.

Keywords Gas dynamics, discontinuous Galerkin, entropy stability

1 Introduction

Accurate simulation of non-equilibrium flows with chemical reactions and internal degrees of freedom is crucial for a multitude of aerospace applications [4, 32, 21]. For such flows, using higher-order discontinuous Galerkin (DG) methods is an attractive prospect, as it enables a more accurate simulation of turbulent effects, lessens the requirements on grid-shock alignment, improves computational efficiency due to data locality, and adds additional solution adaptivity capabilities via p -adaptivity [45, 23, 2, 31, 17, 34]. DG methods are also the natural framework for polynomial expansion-based uncertainty quantification and sensitivity analysis studies [43, 24], an area of research with growing importance, as larger and larger parts of the R&D cycle in aerospace are carried out via simulation tools. The less stringent requirements of DG methods with regards to shock-grid alignment [8] are also useful for uncertainty quantification and sensitivity analysis studies, as those oftentimes require automated simulation of hundreds and thousands of test cases, where automated well-aligned mesh generation is possible only for simple geometries [9].

Development of DG methods suitable for aerospace applications is still an active area of research, as questions of numerical stability, shock capturing, and insufficient numerical diffusion inherent to higher-order methods need to be addressed. Recent achievements in these areas include the DG spectral element method with Legendre-Gauss-Lobatto quadratures (DGSEM-LGL) [11, 12, 39], artificial viscosity approaches [30, 8, 1], shock filtering [30, 3], and subcell limiting techniques [16, 26].

Another question is the choice of the numerical flux functions: from a physics point of view, a crucial desired property of a numerical scheme is entropy conservation [44, 19, 18], especially in the context of DG methods [6, 36, 12]. For summation-by-part (SBP) schemes, this requires entropy-conservative numerical flux functions for the volume and surface fluxes [36, 12]. Augmented by a dissipative surface flux function, the spatial discretization then guarantees entropy stability [6]. Multiple entropy-conservative flux functions have been developed [36], but they usually assume restrictions on the description of the internal energy of the gas flow. Quite often, a constant ratio of specific heats is assumed. Whilst this greatly simplifies the derivation of numerical fluxes, it is not applicable to the kind of high-temperature flows encountered in real-life aerospace applications. In [20], the DG method was applied to the simulation of reacting mixtures with special attention paid to the numerical evaluation of fluxes that avoid generating spurious pressure oscillations. In a recent paper [34], an approach has been proposed to construct entropy stable flux functions for mixtures of molecules with vibrational spectra described by infinite harmonic oscillators. This significantly expands the range of applicability of such entropy-conservative schemes. However, the assumed infinite

*Preprint submitted to Springer Journal of Scientific Computing.

harmonic oscillator model is not the most accurate description of real-life vibrational spectra of molecules. In addition, the approach used to derive the flux functions does not easily generalize to other expressions for internal energy spectra.

In the present work, a new approach to derive of entropy-conservative flux schemes is developed, based on interpolation of the specific heats and entropy integrals. It is applied to the simulation of inviscid high-enthalpy flows over a cylinder, and compared to results obtained with the second order finite volume-based DLR TAU solver [28].

The paper is structured as follows. First, the flow equations for a high-temperature gas flow are presented, the thermodynamic properties of high-temperature gases are discussed, and a brief overview of the impact of various modelling assumptions is given. Then, an entropy-conservative flux is derived for the equations in question, and its computational properties are analyzed. Next, a short overview of the used simulation framework is given and results of numerical simulations are presented. Finally, future work prospects are discussed.

2 Flow equations and thermodynamic properties

We consider a two-dimensional flow of a single-species inviscid gas.

The compressible Euler equations governing such a flow are given by

$$\frac{\partial}{\partial t} \mathbf{u} + \frac{\partial}{\partial x} \mathbf{f}_x + \frac{\partial}{\partial y} \mathbf{f}_y = 0. \quad (1)$$

Here $t \in [0, t_{\max}]$ is the time, x and y are the spatial coordinates in the flow domain $\Omega \subset \mathbb{R}^2$, \mathbf{u} is the vector of conservative variables, and $\mathbf{f}_x, \mathbf{f}_y$ are the inviscid fluxes.

The vector of conservative variables $\mathbf{u} \in \mathbb{R}^4$ is given by

$$\mathbf{u} = (\rho, \rho v_x, \rho v_y, E)^T, \quad (2)$$

where ρ is the density, v_x and v_y are the flow velocities in the x and y directions, and $E = \rho e = \rho \varepsilon_{\text{int}} + \rho v^2/2$ is the total flow energy. Here, e is the specific energy, and ε_{int} is the specific internal energy. The inviscid fluxes are given by

$$\mathbf{f}_x = (\rho v_x, \rho v_x^2 + p, \rho v_x v_y, (E + p)v_x)^T, \quad (3)$$

$$\mathbf{f}_y = (\rho v_y, \rho v_x v_y, \rho v_y^2 + p, (E + p)v_y)^T. \quad (4)$$

Here p is the pressure. We use the ideal gas law to relate pressure, density, and temperature: $p = nkT$, where n is the number density ($n = \rho/m$, where m is the mass of the constituent gas species), k is the Boltzmann constant, and T is the flow temperature. All that is left to fully close the system of equations is a relation between the specific internal energy and the temperature.

2.1 Internal energy models

We now consider several models for $\varepsilon_{\text{int}}(T)$. The simplest case is that of the calorically perfect gas, where $\varepsilon_{\text{int}}(T) = c_v T$, where c_v is the constant-valued specific heat at constant volume. The ratio of specific heats $\gamma = (c_v + k/m)/c_v$ in that case is also temperature-independent. The calorically perfect gas case, especially with $c_v = 5/2 k/m$ (corresponding $\gamma = 1.4$), is the standard one in a large amount of literature concerned with CFD methods in general and entropy-conservative formulations in particular, and we do not consider it in detail.

In the present work, we assume that our gas consists of diatomic molecules, which possess only rotational and vibrational degrees of freedom. That is, we neglect the impact of electronic excitation: $\varepsilon_{\text{int}} = \varepsilon_{\text{tr}} + \varepsilon_{\text{rot}} + \varepsilon_{\text{vibr}}$, where $\varepsilon_{\text{tr}} = \frac{3}{2} kT/m$ is the specific translational energy, and ε_{rot} and $\varepsilon_{\text{vibr}}$ are the specific rotational and vibrational energies, respectively. Moreover, we assume a “rigid rotor” model [32]), that is, that the rotational and vibrational degrees of freedom are uncoupled. We also assume that the rotational mode is fully excited, leading to $\varepsilon_{\text{rot}} = kT/m$. As a consequence, the specific heat of the rotational degrees of freedom simplifies to $c_{v,\text{rot}} = k/m$. For a more detailed discussion of the validity of these assumptions, at least with regard to viscous fluid properties, the reader is referred to [25].

For the vibrational degrees of freedom, we consider the two following models:

1. Infinite harmonic oscillator:

$$\varepsilon_{\text{vibr}} = \frac{k}{m} \frac{\theta_v}{\exp(\frac{\theta_v}{T}) - 1}, \quad c_{v,\text{vibr}} = \frac{k}{m} \frac{\theta_v^2 \exp(\frac{\theta_v}{T})}{T^2 (\exp(\frac{\theta_v}{T}) - 1)^2}, \quad (5)$$

where θ_v is the characteristic vibrational temperature of the molecules.

2. Cut-off oscillator:

$$\begin{aligned} \varepsilon_{\text{vibr}} &= \frac{1}{mZ_{\text{vibr}}} \sum_{i=0}^{i_{\text{max}}} \varepsilon_{v,i} \exp\left(-\frac{\varepsilon_{v,i}}{kT}\right), \quad Z_{\text{vibr}} = \sum_{i=0}^{i_{\text{max}}} \exp\left(-\frac{\varepsilon_{v,i}}{kT}\right), \\ c_{v,\text{vibr}} &= \frac{1}{mZ_{\text{vibr}}} \frac{1}{kT^2} \left(\sum_{i=0}^{i_{\text{max}}} \varepsilon_{v,i}^2 \exp\left(-\frac{\varepsilon_{v,i}}{kT}\right) - \left(\sum_{i=0}^{i_{\text{max}}} \varepsilon_{v,i} \exp\left(-\frac{\varepsilon_{v,i}}{kT}\right) \right)^2 \right). \end{aligned} \quad (6)$$

Here Z_{vibr} is the vibrational partition function, the summation over i denotes the summation over all the allowed discrete vibrational states, $\varepsilon_{v,i}$ is the vibrational energy of the molecule in vibrational state i , and i_{max} is the maximum allowed vibrational state. Usually this is chosen based on the dissociation energy D of the molecule, such that $\varepsilon_{v,i_{\text{max}}} < D < \varepsilon_{v,i_{\text{max}}+1}$.

In the case of $\varepsilon_{v,i} = (i + \frac{1}{2})k\theta_v$, where θ_v is the characteristic vibrational temperature of the molecular species, one obtains the *cut-off harmonic oscillator model*. In case a non-linear dependence of the vibrational energy on the level number is assumed, one obtains a so-called *cut-off anharmonic oscillator model*. In the present work, second-order terms are considered in the case of the anharmonic oscillator model: $\varepsilon_{v,i} = (i + \frac{1}{2})k\theta_v - (i + \frac{1}{2})^2 k\theta_{v,\text{anh}}$, where $\theta_{v,\text{anh}}$ is the characteristic temperature of the anharmonic correction.

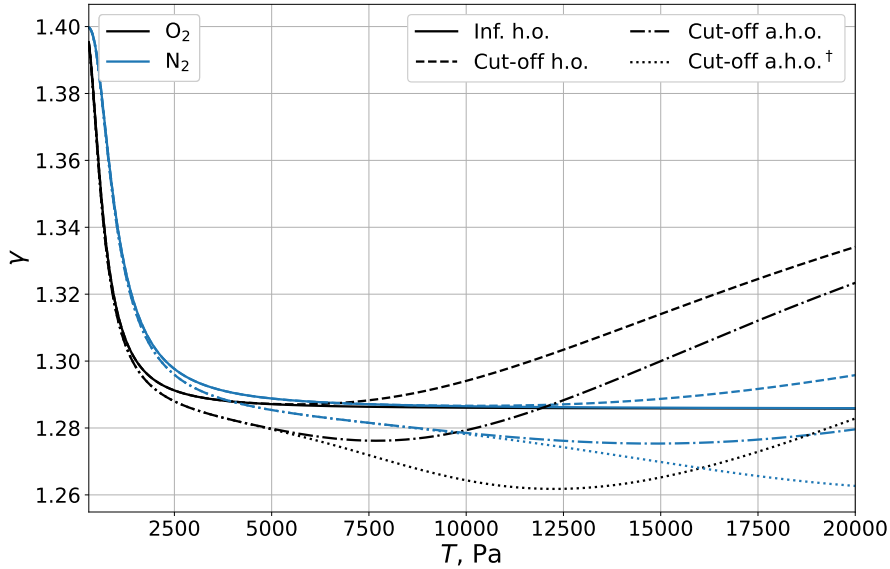


Figure 1: The heat capacity ratio γ as a function of temperature for different models of the vibrational energy spectrum of oxygen (black lines) and nitrogen (blue lines).

In the present work we consider two molecular species: O_2 and N_2 . For O_2 , the following values were used to determine the vibrational spectrum [5]: a dissociation energy D of 59364 K, a characteristic vibrational temperature θ_v of 2273.5 K, and a characteristic temperature of the anharmonic correction $\theta_{v,\text{anh}}$ of 17.366 K. For N_2 , the following values were used: $D = 113252$ K, $\theta_v = 3393.48$ K, $\theta_{v,\text{anh}}$ of 20.603 K.

Figure 1 shows the impact the choice of the vibrational energy spectrum description has on the thermodynamic properties of the gas (in this case, the heat capacity ratio γ). Four different models are considered: the infinite harmonic oscillator, the cut-off harmonic oscillator, the cut-off anharmonic oscillator with the cut-off determined by the dissociation energy of the molecule D , and the cut-off anharmonic oscillator with the cut-off determined by the vibrational level where the vibrational energy starts decreasing with increasing level number (marked with a dagger sign \dagger on the plot legend). It can be seen that the heat capacity ratio strongly deviates from the room temperature value of 1.4, with all the cut-off models exhibiting non-monotone behaviour. For nitrogen, the effects of vibrational excitation and vibrational spectrum cut-off appear at higher temperatures than for oxygen, due to its higher characteristic vibrational temperature. Note that the presented results do not account for effects such as electronic excitation, which further complicate the thermodynamic behaviour of gases at temperatures higher than 7000-10000 K [29, 5].

2.2 Implementation of internal energy models in a CFD solver

Accounting for internal energy effects in a flow solver involves implementing several functions: 1) one to compute the flow temperature T from the conservative variables, 2) one to compute a specific internal energy given the flow temperature T , 3) one to compute the specific heats given the flow temperature T , and 4) one to compute the flow entropy given the temperature and conservative variables. For multi-species flows and flows with thermal non-equilibrium (multi-temperature flows), these functions have to be extended accordingly to account for all the relevant dependencies on the partial densities and the temperatures of the internal degrees of freedom.

In general, no closed-form expression exists to compute T from ε_{int} . As such, existing packages for high-temperature flow simulation, such as Mutation++ [41], use a non-linear solver to obtain the flow temperature. In the present work, a single-species gas is considered, and an approach based on linear interpolation between tabulated values is used due to the lower computational cost; a discussion of the cost of using a non-linear solver in lieu of the linear interpolation is presented below.

First, reasonable minimum and maximum values of T are chosen, e.g., $T_{\min} = 10$ K, $T_{\max} = 50000$ K, as well as a temperature discretization step ΔT . The full specific internal energy $\varepsilon_{\text{int}} = \varepsilon_{\text{int}}(T)$ is computed over the specified temperature range with the corresponding step in ΔT and stored, as well as the total specific heat $c_v = c_v(T)$. Since one needs a way to obtain the temperature, a primitive variable, from energy, a conservative variable, the minimum and maximum internal energy values are computed as $\varepsilon_{\text{int}} = \varepsilon_{\text{int}}(T_{\min})$, $\varepsilon_{\text{int}} = \varepsilon_{\text{int}}(T_{\max})$, and the number of discretization points is chosen to be the same as for the discretization of the temperature range. Based on this, a uniform energy discretization step $\Delta \varepsilon$ is computed, and for each energy in the range, the corresponding temperature is found using a non-linear solver. As this step is done only once during the initialization of the flow solver, a high accuracy can be used for the non-linear solve, as even for a large number of discretization points, the cost taken up by the pre-processing is negligible compared to the time taken up by the flow simulation itself. With these tabulated arrays, reconstructing temperature from the energy and computing energy and/or specific heat from the temperature requires only finding the closest position in the array. This is achieved via division by the discretization step and subsequent rounding down to an integer, and performing a linear interpolation between the nearest values in the array. In case of a multi-species flow, where the inference of temperature from energy requires solving a non-linear equation, the linear interpolation of energy and specific heats is still utilized in the non-linear solver to avoid a potentially expensive computation of energy and its derivative with respect to the temperature at each iteration.

3 Entropy-conservative flux

Having defined our system of flow equations and its closures, we are interested in developing an entropy-conservative flux function. In this, we follow the methodology of Tadmor [44], with the help of the more generic formulation of the entropy as given in [34].

3.1 Entropy and entropy variables

The physical entropy s is defined as the specific quantity

$$s = \int_0^T \frac{c_v(\tau)}{\tau} d\tau - \frac{k}{m} \ln \rho = \eta(T) - \frac{k}{m}. \quad (7)$$

We will hereafter refer to the $\int_0^T \frac{c_v(\tau)}{\tau} d\tau$ as the “integral part” of the entropy. As it will play a central role in the following derivations, we denote it by $\eta(T)$ to simplify the notation. We also define the mathematical entropy as the volume density $\mathfrak{s} = -\rho s$.

The specific entropy satisfies the entropy balance equation [15]

$$\frac{\partial s}{\partial t} + \mathbf{v} \cdot \nabla s = \sigma \geq 0, \quad (8)$$

where $\mathbf{v} = (v_x, v_x)$ is the velocity vector, and σ is the entropy production. The entropy production σ depends on the physics of the problem being considered, i.e. presence of shockwaves, chemical reactions, etc., and we thus leave it unspecified.

In order to derive an entropy-conservative flux, we first need to compute entropy variables, defined by

$$\omega = \frac{\partial \mathfrak{s}}{\partial \mathbf{u}}. \quad (9)$$

As before, our vector of conservative variables is the following

$$\mathbf{u} = (\rho, \rho v_x, \rho v_y, E)^T = \left(\rho, \rho v_x, \rho v_y, \rho \varepsilon_{\text{int}} + \frac{1}{2} \rho v^2 \right)^T, \quad (10)$$

and we define our vector of primitive variables as

$$\mathbf{z} = (\rho, v_x, v_y, T)^T. \quad (11)$$

Using the chain rule [13], we can write the entropy variable vector

$$\boldsymbol{\omega} = \frac{\partial \mathbf{s}}{\partial \mathbf{u}} = \frac{\partial \mathbf{s}}{\partial \mathbf{z}} \left(\frac{\partial \mathbf{u}}{\partial \mathbf{z}} \right)^{-1}. \quad (12)$$

Computing the derivatives of the conservative variables w.r.t. the primitive variables is straightforward

$$\frac{\partial \mathbf{u}}{\partial \mathbf{z}} = \begin{pmatrix} 1 & 0 & 0 & 0 \\ v_x & \rho & 0 & 0 \\ v_y & 0 & \rho & 0 \\ \varepsilon_{\text{int}} + \frac{1}{2} v^2 & \rho v_x & \rho v_y & \rho c_v \end{pmatrix} \quad (13)$$

Inverting, we obtain

$$\left(\frac{\partial \mathbf{u}}{\partial \mathbf{z}} \right)^{-1} = \begin{pmatrix} 1 & 0 & 0 & 0 \\ -\frac{v_x}{\rho} & \frac{1}{\rho} & 0 & 0 \\ -\frac{v_y}{\rho} & 0 & \frac{1}{\rho} & 0 \\ \frac{\frac{1}{2} v^2 - \varepsilon_{\text{int}}}{\rho c_v} & -\frac{v_x}{\rho c_v} & -\frac{v_y}{\rho c_v} & \frac{1}{\rho c_v} \end{pmatrix} \quad (14)$$

Making use of the Leibniz integral rule, we get

$$\frac{\partial \mathbf{s}}{\partial \mathbf{z}} = \left(-s + \frac{k}{m}, 0, 0, -\rho \frac{c_v}{T} \right). \quad (15)$$

Applying (12) and omitting any constant terms independent of the flow variables, we obtain the vector of entropy variables.

$$\boldsymbol{\omega} = (\omega_1, \omega_2, \omega_3, \omega_4) = \left(-s(T) + \frac{\varepsilon_{\text{int}}(T) - \frac{1}{2} v^2}{T}, \frac{v_x}{T}, \frac{v_y}{T}, -\frac{1}{T} \right)^T. \quad (16)$$

3.2 Derivation of entropy-conservative flux

The equation for entropy-conserving flux $\mathbf{F}^{\text{num}, EC, j} \in \mathbb{R}^4$ in spatial direction j ($j = x, y$) is given by the following compatibility condition [44]:

$$[\![\boldsymbol{\omega}^T]\!] \cdot \mathbf{F}^{\text{num}, EC, j} - [\![\psi_j]\!] = 0, \quad (17)$$

where $[\![a]\!] = a_+ - a_-$ is the jump in the value of a flow variable a , and a_- and a_+ denote the values of a flow variable a at two points between which the flux is computed. The flux potentials are given by [34]:

$$\psi_j = \frac{k}{m} \rho v_j. \quad (18)$$

To obtain the flux $\mathbf{F}^{\text{num}, EC, j}$, we need to write $[\![\boldsymbol{\omega}]\!]$ and $[\![\psi_j]\!]$ in terms of jumps in the primitive variables

$$[\![\boldsymbol{\omega}]\!] = A(\mathbf{z}_-, \mathbf{z}_+) \cdot [\![\mathbf{z}]\!], \quad A(\mathbf{z}_-, \mathbf{z}_+) \in \mathbb{R}^{4 \times 4}, \quad (19)$$

$$[\![\psi_j]\!] = B(\mathbf{z}_-, \mathbf{z}_+) \cdot [\![\mathbf{z}]\!], \quad B(\mathbf{z}_-, \mathbf{z}_+) \in \mathbb{R}^{1 \times 4}. \quad (20)$$

Here $A(\mathbf{z}_-, \mathbf{z}_+)$ and $B(\mathbf{z}_-, \mathbf{z}_+)$ are matrices dependent on the values of the primitive variables at the two points between which the flux is computed. The compatibility condition (17) can be rewritten as

$$\left((\mathbf{F}^{\text{num}, EC, j})^T \cdot A(\mathbf{z}_-, \mathbf{z}_+) - B(\mathbf{z}_-, \mathbf{z}_+) \right) \cdot [\![\mathbf{z}]\!] = 0, \quad \forall [\![\mathbf{z}]\!] \in \mathbb{R}^4. \quad (21)$$

Once $A(\mathbf{z}_-, \mathbf{z}_+)$ and $B(\mathbf{z}_-, \mathbf{z}_+)$ have been found, $\mathbf{F}^{\text{num}, EC, j}$ can be computed as

$$\mathbf{F}^{\text{num}, EC, j} = (A^{-1}(\mathbf{z}_-, \mathbf{z}_+) B(\mathbf{z}_-, \mathbf{z}_+))^T. \quad (22)$$

In order to obtain rewrite the jumps in the entropy variables in terms of jumps in the primitive variables, we first need to introduce the following averaging operators [36]

$$\{\{a\}\} = \frac{1}{2} (a_- + a_+), \quad (23)$$

$$\{\{a\}\}_{\text{geo}} = \sqrt{a_- a_+}, \quad (24)$$

$$\{\{a\}\}_{\log} = \frac{a_+ - a_-}{\log a_+ - \log a_-}. \quad (25)$$

Then, the following relations hold [36]:

$$\llbracket ab \rrbracket = \{\{a\}\} \llbracket b \rrbracket + \{\{b\}\} \llbracket a \rrbracket, \quad (26)$$

$$\llbracket \frac{a}{b} \rrbracket = -\frac{\{\{a\}\}}{\{\{b\}\}_{\text{geo}}^2} \llbracket b \rrbracket + \left\{ \left\{ \frac{1}{b} \right\} \right\} \llbracket a \rrbracket, \quad (27)$$

$$\llbracket \log a \rrbracket = \frac{\llbracket a \rrbracket}{\{\{a\}\}_{\log}}. \quad (28)$$

Let us write out the jumps for $\omega_2, \omega_3, \omega_4$ (as defined by (16)), as their derivation is straightforward and does not require any additional discussion. We find

$$\llbracket \omega_2 \rrbracket = \{\{v_x\}\} \llbracket \frac{1}{T} \rrbracket + \left\{ \left\{ \frac{1}{T} \right\} \right\} \llbracket v_x \rrbracket = -\{\{v_x\}\} \frac{1}{\{\{T\}\}_{\text{geo}}^2} \llbracket T \rrbracket + \left\{ \left\{ \frac{1}{T} \right\} \right\} \llbracket v_x \rrbracket. \quad (29)$$

By analogy we obtain

$$\llbracket \omega_3 \rrbracket = -\{\{v_y\}\} \frac{1}{\{\{T\}\}_{\text{geo}}^2} \llbracket T \rrbracket + \left\{ \left\{ \frac{1}{T} \right\} \right\} \llbracket v_y \rrbracket. \quad (30)$$

Finally, for $\llbracket \omega_4 \rrbracket$ we get

$$\llbracket \omega_4 \rrbracket = \frac{1}{\{\{T\}\}_{\text{geo}}^2} \llbracket T \rrbracket. \quad (31)$$

Let us now focus the attention on ω_1 , taking into account the definition of entropy (7).

$$\begin{aligned} \llbracket \omega_1 \rrbracket &= -\llbracket s \rrbracket + \llbracket \frac{\varepsilon_{\text{int}}}{T} \rrbracket - \llbracket \frac{v_x^2 + v_y^2}{2T} \rrbracket \\ &= -\llbracket s \rrbracket - \frac{\{\{\varepsilon_{\text{int}}\}\}}{\{\{T\}\}_{\text{geo}}^2} \llbracket T \rrbracket + \left\{ \left\{ \frac{1}{T} \right\} \right\} \llbracket \varepsilon_{\text{int}} \rrbracket + \frac{\{\{v_x^2\}\} + \{\{v_y^2\}\}}{2 \{\{T\}\}_{\text{geo}}^2} \llbracket T \rrbracket \\ &\quad - \left\{ \left\{ \frac{1}{T} \right\} \right\} \{\{v_x\}\} \llbracket v_x \rrbracket - \left\{ \left\{ \frac{1}{T} \right\} \right\} \{\{v_y\}\} \llbracket v_y \rrbracket \\ &= -\llbracket \eta(T) \rrbracket + \frac{k}{m} \frac{\llbracket \rho \rrbracket}{\{\{\rho\}\}_{\log}} - \frac{\{\{\varepsilon_{\text{int}}\}\}}{\{\{T\}\}_{\text{geo}}^2} \llbracket T \rrbracket + \left\{ \left\{ \frac{1}{T} \right\} \right\} \llbracket \varepsilon_{\text{int}} \rrbracket \\ &\quad + \frac{\{\{v_x^2\}\} + \{\{v_y^2\}\}}{2 \{\{T\}\}_{\text{geo}}^2} \llbracket T \rrbracket - \left\{ \left\{ \frac{1}{T} \right\} \right\} \{\{v_x\}\} \llbracket v_x \rrbracket - \left\{ \left\{ \frac{1}{T} \right\} \right\} \{\{v_y\}\} \llbracket v_y \rrbracket. \end{aligned} \quad (32)$$

All that is left is to express the jumps in $\eta(T)$ and $\varepsilon_{\text{int}}(T)$ in terms of jumps in T . At first this seems impossible unless some specific expressions for $c_v(T)$ and ε_{int} are provided. Even then, a closed-form solution is not necessarily available. For the simplest case of an infinite harmonic oscillator [34], the resulting flux formulae are quite complex and involve hyperbolic functions. Another approach is to use the NASA polynomials [29], which approximate specific heats as polynomials in T and $1/T$. The polynomial fits for entropies and enthalpies are obtained via simple analytical integration. One can plug in the polynomial approximations into (32) and obtain a closed-form expression for the jump in ω_1 using the relevant chain rules, which is the procedure employed in [13]. The drawback of the approach is that for each internal energy model, a new set of fits has to be performed as the coefficients given by NASA take into account effects such as anharmonicity, electronic excitation, etc. Moreover, in thermally non-equilibrium multi-temperature flows, additional fits for the vibrational components of the internal energies need to be provided.

However, we can formally write out the jumps in $\eta(t)$ and ε_{int} using the mean value theorem:

$$\llbracket \eta(T) \rrbracket = \int_0^{T_+} \frac{c_v(\tau)}{\tau} d\tau - \int_0^{T_-} \frac{c_v(\tau)}{\tau} d\tau = \int_{T_-}^{T_+} \frac{c_v(\tau)}{\tau} d\tau = \llbracket T \rrbracket \frac{c_v(T^*)}{T^*}, \quad (33)$$

$$\llbracket \varepsilon_{\text{int}} \rrbracket = \int_0^{T_+} c_v(\tau) d\tau - \int_0^{T_-} c_v(\tau) d\tau = \int_{T_-}^{T_+} c_v(\tau) d\tau = \llbracket T \rrbracket c_v(T^{**}). \quad (34)$$

Here T^* , T^{**} are some values of the temperature in the interval $[\min(T_-, T_+), \max(T_-, T_+)]$. But how do we find the values $c_v(T^*)/T^*$, $c_v(T^{**})$?

The following algorithm is proposed: given \mathbf{u}_+ , \mathbf{u}_- , we first compute $\llbracket \varepsilon_{\text{int}} \rrbracket$ and $\llbracket \eta(T) \rrbracket$. The jump in the internal energy can be computed explicitly. To compute the jump in the integral part of the entropy $\eta(T)$, we pre-compute tabulated values of $\eta(T)$ with a step size of ΔT and store them. Thus, once we convert the conservative variables to the primitive variables, we obtain T_+ and T_- , and use them to find via linear interpolation the jump in $\eta(T)$. Since we already know $\llbracket T \rrbracket$, we simply divide the left-hand sides of (33), (34) by $\llbracket T \rrbracket$ and obtain the required values.

Thus, we can write out the final expression for $\llbracket \omega_1 \rrbracket$:

$$\begin{aligned} \llbracket \omega_1 \rrbracket = & -\llbracket T \rrbracket \frac{c_v(T^*)}{T^*} + \frac{k}{m} \frac{\llbracket \rho \rrbracket}{\{\{\rho\}\}_{\log}} - \frac{\{\{\varepsilon_{\text{int}}\}\}}{\{\{T\}\}_{\text{geo}}^2} \llbracket T \rrbracket + \left\{ \left\{ \frac{1}{T} \right\} \right\} c_v(T^{**}) \llbracket T \rrbracket \\ & + \frac{\{\{v_x^2\}\} + \{\{v_y^2\}\}}{2 \{\{T\}\}_{\text{geo}}^2} \llbracket T \rrbracket - \left\{ \left\{ \frac{1}{T} \right\} \right\} \{\{v_x\}\} \llbracket v_x \rrbracket - \left\{ \left\{ \frac{1}{T} \right\} \right\} \{\{v_y\}\} \llbracket v_y \rrbracket. \end{aligned} \quad (35)$$

Substituting into (17) and solving for the flux components, we obtain two entropy-conserving flux vectors (in the x and y spatial directions) for the conservative variables:

$$F_{\rho}^{\text{num},x} = \{\{\rho\}\}_{\log} \{\{v_x\}\}, \quad (36)$$

$$F_{\rho v_x}^{\text{num},x} = F_{\rho}^{\text{num},x} \{\{v_x\}\} + \frac{k}{m} \frac{\{\{\rho\}\}}{\{\{1/T\}\}}, \quad (37)$$

$$F_{\rho v_y}^{\text{num},x} = F_{\rho}^{\text{num},x} \{\{v_y\}\}, \quad (38)$$

$$\begin{aligned} F_E^{\text{num},x} = & F_{\rho}^{\text{num},x} \{\{T\}\}_{\text{geo}}^2 \left(\frac{c_v(T^*)}{T^*} - \left\{ \left\{ \frac{1}{T} \right\} \right\} c_v(T^{**}) \right) \\ & + F_{\rho}^{\text{num},x} \left(\{\{\varepsilon_{\text{int}}\}\} - \frac{\{\{v_x^2\}\} + \{\{v_y^2\}\}}{2} \right) \\ & + \{\{v_x\}\} F_{\rho v_x}^{\text{num},x} + \{\{v_y\}\} F_{\rho v_y}^{\text{num},x}. \end{aligned} \quad (39)$$

In the y direction:

$$F_{\rho}^{\text{num},y} = \{\{\rho\}\}_{\log} \{\{v_y\}\}, \quad (40)$$

$$F_{\rho v_x}^{\text{num},y} = F_{\rho}^{\text{num},y} \{\{v_x\}\}, \quad (41)$$

$$F_{\rho v_y}^{\text{num},y} = F_{\rho}^{\text{num},y} \{\{v_y\}\} + \frac{k}{m} \frac{\{\{\rho\}\}}{\{\{1/T\}\}}, \quad (42)$$

$$\begin{aligned} F_E^{\text{num},y} = & F_{\rho}^{\text{num},y} \{\{T\}\}_{\text{geo}}^2 \left(\frac{c_v(T^*)}{T^*} - \left\{ \left\{ \frac{1}{T} \right\} \right\} c_v(T^{**}) \right) \\ & + F_{\rho}^{\text{num},y} \left(\{\{\varepsilon_{\text{int}}\}\} - \frac{\{\{v_x^2\}\} + \{\{v_y^2\}\}}{2} \right) \\ & + \{\{v_x\}\} F_{\rho v_x}^{\text{num},y} + \{\{v_y\}\} F_{\rho v_y}^{\text{num},y}. \end{aligned} \quad (43)$$

This concludes the derivation of the entropy-conservative numerical flux for the case of a single-species gas with arbitrary internal energies.

3.3 Limiting case

We can check that in the case of $c_v = \text{const}$, the formulas reduce to the fluxes as given by expression (75) in [36]. For the density and velocity fluxes, this is immediately evident if one uses $R_{\text{specific}}T$ instead of T as the variable, where $R_{\text{specific}} = \frac{k}{m}$. All that remains is to simplify the expressions for the energy flux (we only consider the flux in the y direction, the derivation for the x direction is done by analogy). For constant c_v , we have that $\eta(T_+) - \eta(T_-) = \int_{T_-}^{T_+} c_v/\tau d\tau = c_v(\log T_+ - \log T_-)$. We can therefore write that $T^* = \{\{T\}\}_{\log}$. We also have that $\{\{\varepsilon_{\text{int}}\}\} = c_v \{\{T\}\}$. Therefore, we can re-write expression (43) as

$$\begin{aligned} F_E^{\text{num},y} &= F_\rho^{\text{num},y} c_v \left(\frac{\{\{T\}\}_{\text{geo}}^2}{\{\{T\}\}_{\log}} - \{\{T\}\}_{\text{geo}}^2 \left\{ \left\{ \frac{1}{T} \right\} \right\} + \{\{T\}\} \right) \\ &\quad - F_\rho^{\text{num},y} \frac{\{\{v_x^2\}\} + \{\{v_y^2\}\}}{2} \\ &\quad + \{\{v_x\}\} F_{\rho v_x}^{\text{num},y} + \{\{v_y\}\} F_{\rho v_y}^{\text{num},y}. \end{aligned} \quad (44)$$

The term $-\{\{T\}\}_{\text{geo}}^2 \left\{ \left\{ \frac{1}{T} \right\} \right\} + \{\{T\}\}$ can easily be shown to be equal to 0. Finally, using the definition of $\gamma = c_p/c_v$ and Mayer's relation $c_p = c_v + k/m$, we can write $k/(m(\gamma - 1))$ instead of c_v . Thus, we obtain the final expression for the energy flux:

$$\begin{aligned} F_E^{\text{num},y} &= F_\rho^{\text{num},y} \left(\frac{k}{m} \frac{1}{\gamma - 1} \frac{\{\{T\}\}_{\text{geo}}^2}{\{\{T\}\}_{\log}} - \frac{\{\{v_x^2\}\} + \{\{v_y^2\}\}}{2} \right) \\ &\quad + \{\{v_x\}\} F_{\rho v_x}^{\text{num},y} + \{\{v_y\}\} F_{\rho v_y}^{\text{num},y}. \end{aligned} \quad (45)$$

This can be seen to be exactly the energy flux as given by Eqn. (75) in [36] (which in turn is based on the flux proposed by Chandrashekar [7]), up to a trivial change of variables from T to $R_{\text{specific}}T$.

This concludes the derivation of an algorithm for computing entropy-conserving flux functions for a gas with an arbitrary internal energy function.

3.4 Algorithm for pre-processing and flux computation

Here, an outline of the overall algorithm for the pre-computation of relevant tabulated values and subsequent estimation of the flux components is presented.

Algorithm 1 shows a pseudocode description of how the necessary tabulated quantities are precomputed. To distinguish between the flow variables arrays of tabulated values, we subscript the latter with A . All of the arrays T_A , E_A , $E_{u,A}$, $c_{v,A}$, $T_{\text{inv},A}$, η_A are of size $N + 1$ and store the tabulated values. The user has to provide the minimum and maximum values of the temperature range, as well as the temperature step ΔT . The functions for computation of the specific internal energy ε_{int} and the specific heat $c_{v,\text{int}}$ from temperature are assumed to be known. It is usually not possible to compute the temperature from the internal energy, and thus, some non-linear solver needs to be used to populate the $T_{\text{inv},A}$ array (by computing temperature from the uniformly discretized energy range $E_{u,A}$). While higher-order integration methods can be implemented instead of Simpson's rule, the linear interpolation of specific heats and temperature (in dependence on energy) also places bounds on the minimum error achievable with the scheme. In general, it is assumed that the discretization step ΔT is chosen such that the error due to the approximations used is extremely small even using the proposed simple integration and interpolation rules.

Algorithm 2 shows the computation of the quantities required for the calculation of the fluxes as given by Eqns. (36)–(43). First, the temperature is computed from the internal energy, and is then used to approximate the specific heats and integral parts of the entropy of the left and right states. In order to avoid division by zero, in case the temperatures of the left and right states are close (as defined by some prescribed tolerance r , for example $r = 0.5\Delta T$), the jumps in the integral part of the entropy and internal energy are simply replaced by their derivatives evaluated at $T = (T_{ll} + T_{rr})/2$. In a more general scenario (e.g., a multi-species flow), the linear interpolation of temperature from the energy would need to be replaced by a call to a non-linear solver.

3.5 Computational complexity and error analysis

We now analyze the computational cost of the algorithm and the error due to interpolation. Compared to the case of constant c_v , for each entropy-conservative flux computation, the following additional computations are required:

Algorithm 1 Pre-computation of tabulated quantities

Require: $T_{min} > 0, T_{max} > T_{min}, \Delta T > 0, \varepsilon_{vibr}(T), T(\varepsilon_{int})$

$N \leftarrow \lfloor (T_{max} - T_{min}) / \Delta T \rfloor$ ▷ Compute number of array elements

$E_{min} \leftarrow \frac{1}{m} \left(\frac{5}{2} k T_{min} + \varepsilon_{vibr}(T_{min}) \right)$ ▷ Compute minimum internal energy

$E_{max} \leftarrow \frac{1}{m} \left(\frac{5}{2} k T_{max} + \varepsilon_{vibr}(T_{max}) \right)$ ▷ Compute maximum internal energy

$\Delta E \leftarrow (E_{max} - E_{min}) / N$ ▷ Compute uniform internal energy spacing

for $i = 0, \dots, N$ **do**

$T_A[i] \leftarrow T_{min} + i \Delta T$ ▷ Set element of uniformly spaced temperature array

$E_{u,A}[i] \leftarrow E_{min} + i \Delta E$ ▷ Set element of uniformly spaced energy array

$E_A[i] \leftarrow \varepsilon_{int}(T_A[i])$ ▷ Compute and set element of energy array

$c_{v,A}[i] \leftarrow c_v(T_A[i])$ ▷ Compute and set element of specific heat array

$T_{inv,A}[i] \leftarrow T(E_{u,A}[i], T_A[i])$ ▷ Compute temperature from energy with a non-linear solver using $T_A[i]$ as a starting guess

if i is 0 **then**

$\eta_A[i] \leftarrow 0$

else

$T_a \leftarrow T_A[i - 1]$

$T_b \leftarrow T_A[i]$

$T_{ab} \leftarrow \frac{1}{2} (T_a + T_b)$ ▷ Compute endpoints for integration via Simpson's rule

$\eta_A[i] \leftarrow \eta_A[i - 1] + \frac{\Delta T}{6} (c_v(T_a)/T_a + 4c_v(T_{ab})/T_{ab} + c_v(T_b)/T_b)$ ▷ Compute integral part of entropy using Simpson's rule

end if

end for

Algorithm 2 Computation of quantities necessary for calculation of fluxes

Require: $\rho_-, v_{x,-}, v_{y,-}, \varepsilon_{int,-}, \rho_+, v_{x,+}, v_{y,+}, \varepsilon_{int,+}$

for $i = -, +$ **do** ▷ Compute relevant quantities for left and right states

$f_{e,i} \leftarrow (\varepsilon_{int,i} - E_{min}) / \Delta E$

$I_{e,i} \leftarrow \lfloor f_{e,i} \rfloor$ ▷ Find position in array of energy

$f_{e,i} \leftarrow f_{e,i} - I_{e,i}$ ▷ Find linear interpolation coefficient

$T_i \leftarrow (1 - f_{e,i}) \cdot T_{inv,A}[I_{e,i}] + f_{e,i} \cdot T_{inv,A}[I_{e,i} + 1]$ ▷ Find temperature from energy

$f_{T,i} \leftarrow (T_i - T_{min}) / \Delta T$

$I_{T,i} \leftarrow \lfloor f_{T,i} \rfloor$ ▷ Find position in array of temperature

$f_{T,i} \leftarrow f_{T,i} - I_{T,i}$ ▷ Find linear interpolation coefficient

$c_{v,i} \leftarrow (1 - f_{T,i}) \cdot c_{v,A}[I_{T,i}] + f_{T,i} \cdot c_{v,A}[I_{T,i} + 1]$ ▷ Find specific heat from temperature

$\eta_i \leftarrow (1 - f_{T,i}) \cdot \eta_A[I_{T,i}] + f_{T,i} \cdot \eta_A[I_{T,i} + 1]$ ▷ Find integral part of entropy from temperature

end for

if $|T_+ - T_-| < r$ **then** ▷ r is a small fixed tolerance to avoid division by 0

$\bar{T} \leftarrow (T_+ + T_-) / 2$

$f_{\bar{T}} \leftarrow (\bar{T} - T_{min}) / \Delta T$

$I_{\bar{T}} \leftarrow \lfloor f_{\bar{T}} \rfloor$

$f_{\bar{T}} \leftarrow f_{\bar{T}} - I_{\bar{T}}$

$\bar{c}_v \leftarrow (1 - f_{\bar{T}}) \cdot c_{v,A}[I_{\bar{T}}] + f_{\bar{T}} \cdot c_{v,A}[I_{\bar{T}} + 1]$ ▷ Find specific heat from temperature

$c_v(T^*) / T^* \leftarrow \bar{c}_v / \bar{T}$

$c_v(T^{**}) \leftarrow \bar{c}_v$

else

$c_v(T^*) / T^* \leftarrow (\eta_+ - \eta_-) / (T_+ - T_-)$

$c_v(T^{**}) \leftarrow (\varepsilon_{int,+} - \varepsilon_{int,-}) / (T_+ - T_-)$

end if

1. computation of T_+ , T_- ,
2. calculation of $\llbracket \varepsilon_{\text{int}} \rrbracket$, $\llbracket \eta(T) \rrbracket$,
3. calculation of $c_v(T^*)/T^*$, $c_v(T^{**})$.

In the following analysis we disregard the cost of the computation of temperature from energy, as in the present work a single-species formulation is assumed. This allows for significantly faster computation as compared to using a non-linear solver, which is required in the more general multi-species case.

Computation of a linear interpolation of a function of some variable x given x requires the following floating-point operations: 1 subtraction, 1 division operation and 1 rounding operation (to get the index in the tabulated array), 1 subtraction operation (to get the relative position between the two closest array values), 2 multiplication operations, 1 subtraction and 1 summation operation (to perform the linear interpolation). In addition, 2 array access operations are needed. In total, 1 division, 1 round-off, 2 multiplications, 1 summation, 3 subtractions, and 2 array accesses are required. We need to perform linear interpolation twice: to compute $\eta(T_+)$ and $\eta(T_-)$. Whilst the pseudocode in Algorithm 2 contains 6 linear interpolations (temperature T , $c_v(T)$, and $\eta(T)$ for each of the left and right states), the specific heat is required only in case the temperatures of the left and right states are very close (in which case interpolation of the integral part of the entropy is not needed; vice versa, if $|T_+ - T_-| > r$, the interpolation of the specific heats is not required. Therefore, with careful handling of the possible cases, no more than 4 linear interpolations are needed for any given pair of neighbouring flow states. Additionally, as already stated, the interpolation of temperature is neglected in the present analysis. Two additional subtractions are needed to compute the jumps in energy and the integral part of the entropy. Finally, 2 division operations are needed to compute $c_v(T^*)/T^*$, $c_v(T^{**})$.

So in total, we require 12 subtractions/additions, 4 multiplications, 2 round-offs, 4 divisions, and 4 array accesses. Two of the divisions can be re-formulated as multiplications, as the division is by a constant value of ΔT that is set at the start of the simulation. In that case, the number of floating-point operations is 12 subtractions/additions, 6 multiplications, 2 round-offs, 2 divisions.

Having replaced division by multiplication where possible, the worst case cost of the flux evaluation is then 120 cycles, based on data on Ivy Bridge processor family latencies [10]. The formulation in [34] requires at least three exponentiations (each 68 cycles), two logarithms (each 90 cycles), 6 multiplications, 1 division, leading to an approximate cost of 424 cycles, approximately 3.5 as many cycles as the formulation in the present work. Again, it is important to note that in both cases, the cost of computing the temperature from the energy is neglected. Another factor not considered in the present analysis is the role of cache effects. The approach proposed in the present work requires storing several large one-dimensional arrays of floating point numbers, which are being accessed at every step of the simulation, which could lead to frequent loading and eviction of data from the CPU cache.

The sources of numerical error in the presented flux formulation are

1. Error in temperature from linear interpolation (computing temperature from energy)
2. Error in approximation of $\eta(T)$ when storing the tabulated values (dependent on quadrature rule used in the pre-processing step)
3. Error in the linear interpolation of the integral $\eta(T)$ between the tabulated values.

For the linear interpolation used in the present work, the error in the estimation of temperature is of second order in ΔE . The error in the tabulated values of $\eta(T)$ is of fourth order in ΔT (assuming Simpson's rule is used). Finally, the error in the linear interpolation of the integral part of the entropy is of second order in ΔT . A numerical investigation of the errors in the flux evaluation (and the impact of different error sources), along with an analysis of the computational cost of the flux computation algorithm, is presented in the following section.

4 Numerical results

To verify the developed flux and apply it to simulation of two-dimensional high-speed flows, the developed algorithms for computation of flow properties and fluxes were implemented in Trixi.jl [40, 38], a modular framework for solving systems of hyperbolic equations using the DGSEM method. The strong stability preserving Runge-Kutta method SSPRK43 was used for time integration, as provided by the DifferentialEquations.jl library [35]. The simulation code is publicly available on Github [33].

4.1 Comparison to exact expressions for fluxes

First, the developed flux is compared to existing entropy-conserving fluxes for cases where exact expressions for the latter are available. We compare to the flux of Chandrashekar [7] in the case of a calorically perfect gas, and to the flux of Peyvan et al. [34] in the case of a gas described by the infinite harmonic oscillator model.

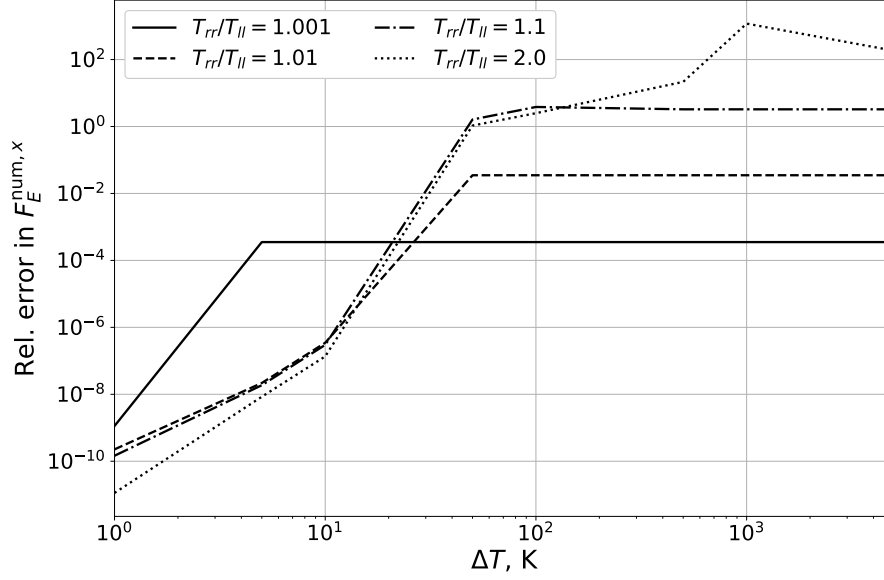


Figure 2: Relative error in the energy flux for different temperature jumps as a function of the discretization step ΔT , $\gamma = 1.4$.

4.1.1 Calorically perfect gas

In the case of a calorically perfect gas, the error due to interpolation of temperature is exactly zero, as in that case temperature is a linear function of energy and the inversion is exact. Fig. 2 shows the error in the evaluation of the flux for the energy $F_E^{\text{num},x}$ using Eqn. 39 computed via Algorithm 2 for various choices of ΔT , as compared to the exact expression for the calorically perfect gas as given by Eqn. 45. In this case, $c_v = \frac{5}{2} \frac{k}{m}$ was assumed, corresponding to an adiabatic index $\gamma = 1.4$. The densities and velocities of the left and right states were assumed to be equal ($\rho_{ll} = \rho_{rr} = 3.8485 \cdot 10^{-3} \text{ kg/m}^3$, $v_{x,ll} = v_{x,rr} = 1000 \text{ m/s}$, $v_{y,ll} = v_{y,rr} = 500.0 \text{ m/s}$), the temperature of the left state T_{ll} was taken to be 1000 K and four different temperature jumps were considered: $T_{rr}/T_{ll} = 1.001$, $T_{rr}/T_{ll} = 1.01$, $T_{rr}/T_{ll} = 1.1$, and $T_{rr}/T_{ll} = 2.0$. The tolerance r used in Alg. 2 was taken to be equal to $\Delta T/2$; that is, for $|T_{rr} - T_{ll}| < r$ the specific heat was simply evaluated at the midpoint $(T_{rr} + T_{ll})/2$, as opposed to using look-up tables for the integral part of the entropy and the internal energy. This is the reason why on Fig. 2 the error levels out after a certain ΔT — as soon as ΔT becomes large enough that $|T_{rr} - T_{ll}| < \Delta T/2$, the flux computation simply computes the specific heat at the mean temperature, and is thus no longer affected by the discretization error in the temperature. Since a constant γ is used for this test case, there is no error due to the computation of temperature from the energy. It can be seen that for the case of a reasonable discretization step (i.e., less than 10 K), the error is on the order of 10^{-8} – 10^{-4} and decreases rapidly with smaller ΔT .

4.1.2 Infinite harmonic oscillator

Next, we compare the energy flux (39) to the flux derived in [34] for the case of the infinite harmonic oscillator model. The gas was assumed to be molecular oxygen (with a molecular mass $m = 5.3134 \times 10^{-26} \text{ kg}$), and a characteristic vibrational temperature of $\theta_v = 2273.5 \text{ K}$ was used. We consider the following three scenarios:

1. Comparison of the energy flux (39) to the flux derived in [34] assuming the temperatures are known exactly (no impact of error in the temperature estimation).
2. Comparison of the energy flux (39) to the flux derived in [34] using linear interpolation to infer the temperature from the internal energy for use in (39), but assuming the temperature to be known exactly for the flux from [34], thus treating it as an exact benchmark.

3. Comparison of the flux derived in [34] with an exactly known temperature to its version where the temperature is computed from the internal energy using the Mutation++ library [41].

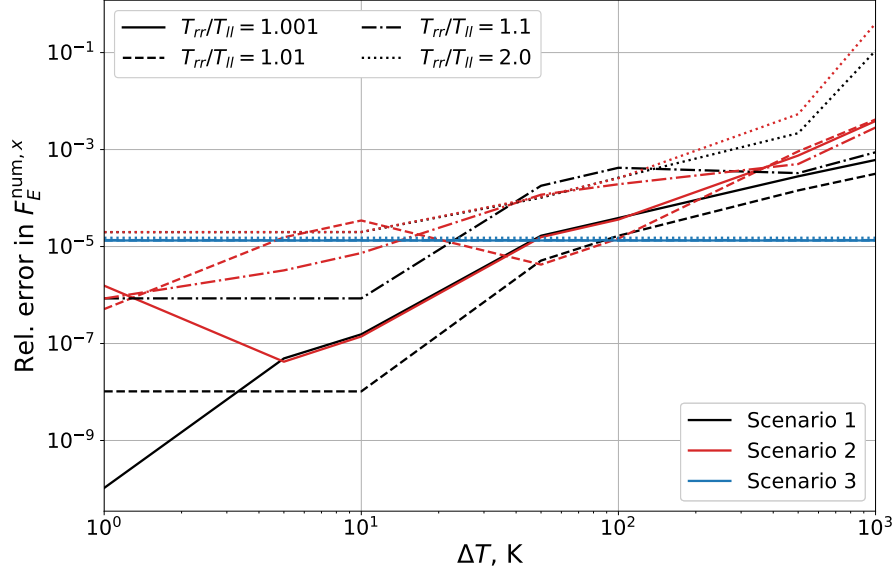


Figure 3: Relative error in the energy flux as a function of the discretization step ΔT , infinite harmonic oscillator. Different line styles correspond to different temperature jumps, different line colors correspond to the different scenarios described above.

Figure 3 shows the relative errors in the energy flux (compared to the flux from [34] assuming exactly known temperatures) for different temperature jumps as a function of the discretization step ΔT . The black lines correspond to scenario 1: exact temperatures are given in the flux functions, and the error is only due to approximation of jumps in the entropy and energy. The red lines correspond to scenario 2: linear interpolation is used to compute the temperature from the energy for use in Eqn. (39). Finally, the blue lines correspond to the error in the flux from [34] arising due to the inference of temperature from the energy using the Mutation++ library. We see that at values of ΔT up to 500 K, the error in the flux is strongly affected by the error due to the inexact estimation of temperature from the energy, at higher values of ΔT , the error in the estimation of the jumps in energy and entropy becomes dominant. Of course, in practice, small discretization values are usually used (1-5 K), in which case the relative error in the flux when comparing it to the exact flux with exactly known temperatures is approximately 10^{-6} – 10^{-5} . When one compares the flux from [34], where temperatures were computed using Mutation++, to its exact version (with no error in the temperature), the relative error is 10^{-5} . As Mutation++ uses a non-linear solver to deduce the temperature, the error is independent of ΔT . Thus, at small values of ΔT , the proposed flux expression (39) achieves excellent error despite using linear interpolation both for estimation of temperature and estimation of the jumps in internal energy and entropy.

4.1.3 Computational cost comparison

We carry out a brief comparison of the computational cost of calculating the flux vector (36)–(39) and the computational cost of calculating the flux vector as given in [34]. Both fluxes were implemented in the Julia programming language. On a i9-13900K processor the computation of the flux vector using Eqns. (36)–(39), including the estimation of temperature from the internal energy using linear interpolation, required 17.8 ns on average, whereas computation of the flux vector as given in [34] without accounting for the cost of inverting the energy to obtain temperature required 26.8 ns on average, approximately 50% more computational time. Estimation of temperatures of the left and right states from the internal energy using the C++ interface of the Mutation++ (compiled using the -O3 compiler flag) library adds another 56 ns of CPU time to each flux evaluation, thus bringing the total time required to compute the flux vector derived in Peyvan et al. [34] to 82.8 ns on average.

For a fairer comparison, the linear interpolation of temperature from energy was replaced by a non-linear Newton-Raphson solver using the same relative tolerance of 10^{-12} as Mutation++, as well as the same starting guess for the temperature T . In that case, evaluation of the flux vector proposed in the present work required 13 ns on average, as the temperature estimation is now performed separately. The computation of the temperatures of the left and right

states from the internal energy required 53 ns on average. Thus, the total cost of evaluating the flux proposed in the present work when a non-linear solver is used to infer the temperatures is on average 66 ns. The flux of Peyvan et al. [34] in conjunction with the Mutation++ library requires approximately 83 ns per evaluation, a 25% increase in computational cost. When the temperature inversion costs are not accounted for, the evaluation of the flux of Peyvan et al. [34] is approximately twice as slow than the computation of the flux (36)–(39).

As a baseline comparison, the flux of Chandrashekar [7] for a calorically perfect gas requires 12 ns per flux evaluation, as the temperature can be computed from the energy via simple analytical inversion, and no look-ups and interpolations are required. Computation of the volume flux is one of the most expensive parts of the solver, with the current implementation in Trixi.jl spending between 50% and 75% of the total run-time computing the volume flux (depending on the polynomial order used in the simulation, with higher orders requiring more flux evaluations). As such, reducing the computational cost of the flux function is crucial to the efficiency of the solver [37]. The flux (36)–(39) derived in the present work thus has been shown have excellent error and computational performance. Moreover, it is important to emphasize again that its performance is independent of the model chosen for the description of the internal energy of the gas, as exact evaluations are performed only during the pre-processing step. It can also be seen that the inversion of energy in order to obtain the temperature comprises the by far most expensive part of the flux evaluation (up to 80% of the total time), although this can be somewhat improved by supplying a good initial guess for the temperature, reducing the number of iterations until convergence.

4.2 Periodic flow

To assess the performance of the developed flux, we consider a two-dimensional test case with periodic boundary conditions, similar to the one investigated in [34]. A square domain $[0, 1] \times [0, 1]$ was assumed. The gas was taken to be molecular nitrogen, with a molecular mass of $m = 4.6517 \times 10^{-26}$ kg and with the vibrational spectrum modelled by an infinite harmonic oscillator model with $\theta_v = 3393.5$ K. The temperature discretization ΔT was taken to be 1 K. The pressure in the domain was taken to be constant as $p = 195256$ Pa, and a velocity vector $\mathbf{v} = (11450; 0)^T$ m/s was assumed. A temperature profile varying in the x direction was prescribed as $T(x) = 9000.0 + 200 \sin(2\pi x)$. A uniform 64×64 grid was used for the discretization of the domain, and 3-rd degree polynomials were used in the DG method. All shock-capturing functions and positivity-preserving limiters were turned off, and the flux (36)–(39) was also used for the interface fluxes (instead of a Riemann solver), to ensure that no stabilization or dissipation schemes can impact the entropy conservation. The total entropy production rate (over all cells in the simulation domain), which can be defined as

$$s_{t,\text{tot}} = \sum \frac{\partial s}{\partial \mathbf{u}} \cdot \frac{\partial \mathbf{u}}{\partial t} \quad (46)$$

was computed via analysis callbacks available in Trixi.jl.

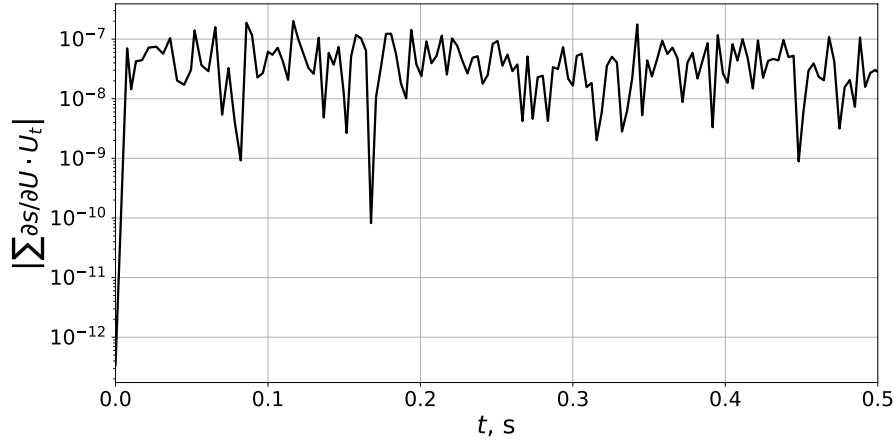


Figure 4: Absolute value of the entropy production rate over the course of the simulation.

Figure 4 shows the total entropy production rate plotted over time. It can be clearly seen that the entropy is not conserved to machine precision, due to the aforementioned errors in the computation of temperature and jumps in the energy and integral part of the entropy; however, the overall magnitude of the entropy production rate is still very small.

4.3 Blast wave

Next, we consider the weak blast wave condition adapted from [16]. The initial conditions are given by

$$\begin{bmatrix} \rho \\ v_x \\ v_y \\ p \end{bmatrix} = \begin{bmatrix} 0.341388 \\ 0.0 \\ 0.0 \\ 101325.0 \end{bmatrix} \text{ if } \sqrt{x^2 + y^2} > 0.5; \quad \begin{bmatrix} \rho \\ v_x \\ v_y \\ p \end{bmatrix} = \begin{bmatrix} 0.399117 \\ 102.5 \cos(\phi) \\ 102.5 \sin(\phi) \\ 126149.6 \end{bmatrix} \text{ else.} \quad (47)$$

Here $\phi = \tan^{-1}(y/x)$. The initial conditions of the problem correspond to a circular-shaped region with a radius of 0.5 m of higher density and pressure with a constant outward radial velocity. As in the previous case, the gas was assumed to be molecular nitrogen, with a vibrational spectrum described by the infinite harmonic oscillator model. A square domain of size $[-2, 2] \times [-2, 2]$ was used, discretized by a uniform 64×64 grid. 3-rd degree polynomials were used in the DG method.

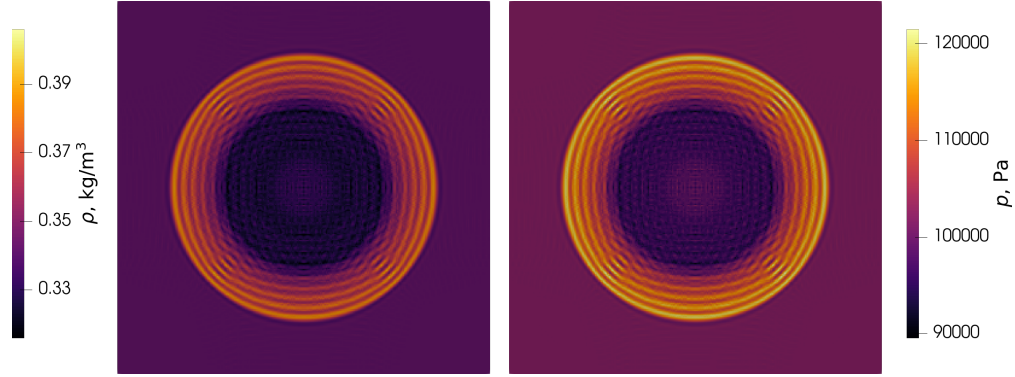


Figure 5: Density (left) and pressure (right) at $t = 0.75$ s for the weak blast wave test case, 64×64 grid.

Figure 5 shows the density and pressure profiles at $t = 0.75$ s. The oscillations in the density and pressure in the radial direction are due to the absence of numerical diffusion in the simulation. The ripples observed in the center of the domain are numerical artifacts due to the use of a coarse uniform Cartesian grid, which is poorly suited for the radially symmetric problem under consideration. Nevertheless, as expected, the simulation is stable, even without dissipative surface fluxes, shock capturing, and/or positivity preserving limiters.

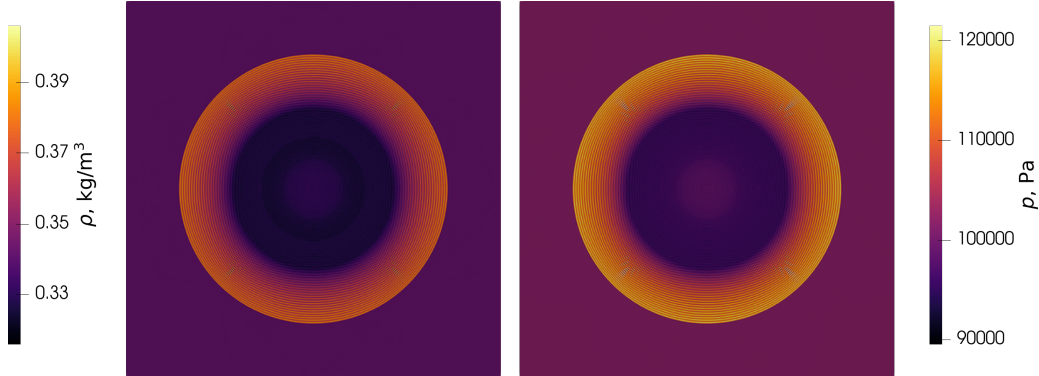


Figure 6: Density (left) and pressure (right) at $t = 0.75$ s for the weak blast wave test case, 256×256 grid.

Figure 6 shows the same simulation on a uniform 256×256 grid. The improved grid resolution can be seen to remedy the ripples in the center of the domain, whereas the oscillations across the blast wave front remain, as no numerical diffusion is applied within the solver.

Figure 7 shows the total entropy production rate plotted over time. Similar to the previous test case, it can be seen that whilst there is an error in the entropy production rate that is larger than machine precision, it does not increase over time and is still of a very small magnitude.

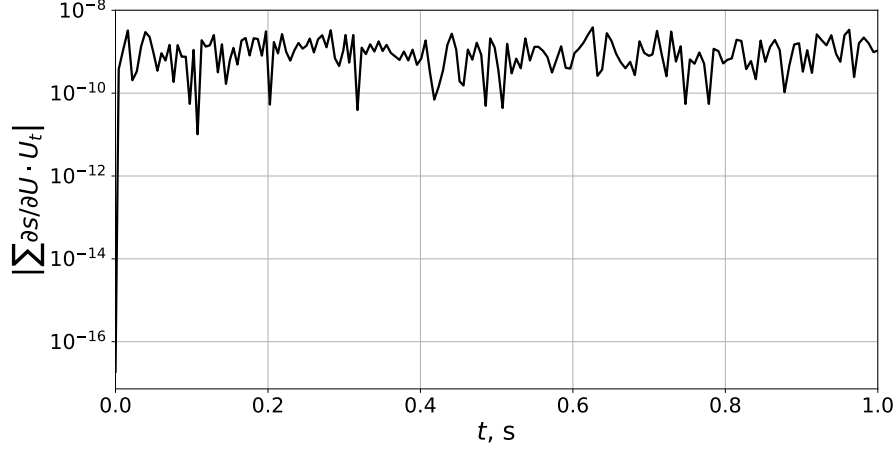


Figure 7: Absolute value of the entropy production rate over the course of the simulation.

4.4 Flow around a cylinder

Finally, we consider a two-dimensional flow around a cylinder. The free-stream parameters were chosen to be $v_\infty = 5956$ m/s, $p_\infty = 476$ Pa, $T_\infty = 901$ K, based on the experimental HEG cylinder test-case [22]; the cylinder diameter is 0.045 m. The gas was assumed to be molecular oxygen with a molecular mass $m = 5.3134 \times 10^{-26}$ kg. The flow speed is approximately Mach 10.5, depending on the chosen model for the internal energy. Two models for the internal energy were considered:

1. Infinite harmonic oscillator with $\theta_v = 2273.5$ K.
2. Cut-off anharmonic oscillator with $\theta_v = 2273.5$ K and $\theta_{v,\text{anh}} = 17.366$ K. The cut-off was performed not based on the dissociation energy of oxygen, but based on the level number where the vibrational energy begins to decrease with increasing vibrational level (as it is given by a quadratic dependence on the level number). This corresponds to 66 vibrational levels accounted for.

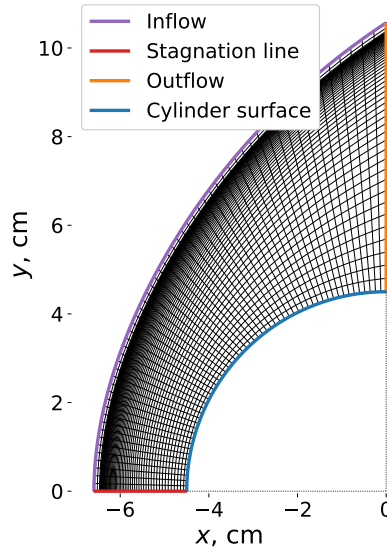


Figure 8: Example of the grid used for the simulations with the infinite harmonic oscillator model.

The simulations were performed on a simple shock-fitted structured 60×60 grid. A single cubic curve was fitted to the shock shape. As it does not fit the shock perfectly, some minor errors in the density and pressure are expected near certain regions of the shock, where the mesh and the shock are not well-aligned. Figure 8 shows an example

of the simulation grid, specifically, the grid used for simulations with the infinite harmonic oscillator model. The origin of the cylinder is located at $(x, y) = (0, 0)$. In the analysis of the simulations presented further below, flow quantities are considered along the stagnation line, given by $y = 0$, and the outflow boundary, given by $x = 0$. The following boundary conditions were applied in the simulation: supersonic inflow at the inflow boundary (highlighted in purple), supersonic outflow for the outflow boundary (highlighted in orange), and slip conditions at the stagnation line (highlighted in red) and cylinder surface (highlighted in blue).

The developed entropy-conserving flux was used for the volume fluxes, and the local Lax-Friedrichs flux was used for the surface fluxes in order to provide sufficient numerical diffusion for the strong shocks present in the flow. The sub-cell shock capturing method of Hennemann et al. [16] was used, along with the positivity-preserving limiter of Zhang and Shu [46].

The DLR TAU solver [28, 14] was used as a benchmark solver for this case with a similar grid and parameters governing the gas properties. The AUSM+ flux [27] was used, along with local time-stepping and a first-order implicit Backward Euler solver. In the case of the infinite harmonic oscillator and cut-off anharmonic oscillators the input thermodynamic data files for DLR TAU were adjusted to provide agreement between the thermodynamic data implemented in Trixi and the data used in the TAU code. Yet there remained some discrepancies in the specific heats. Therefore, to first verify the basic solver components (discretization, shock-capturing, limiting, etc.) for the considered flow, the simplified case with a constant specific heat was considered. The gas was assumed to have the molecular mass of nitrogen, and a heat capacity ratio $\gamma = 1.4$ was assumed.

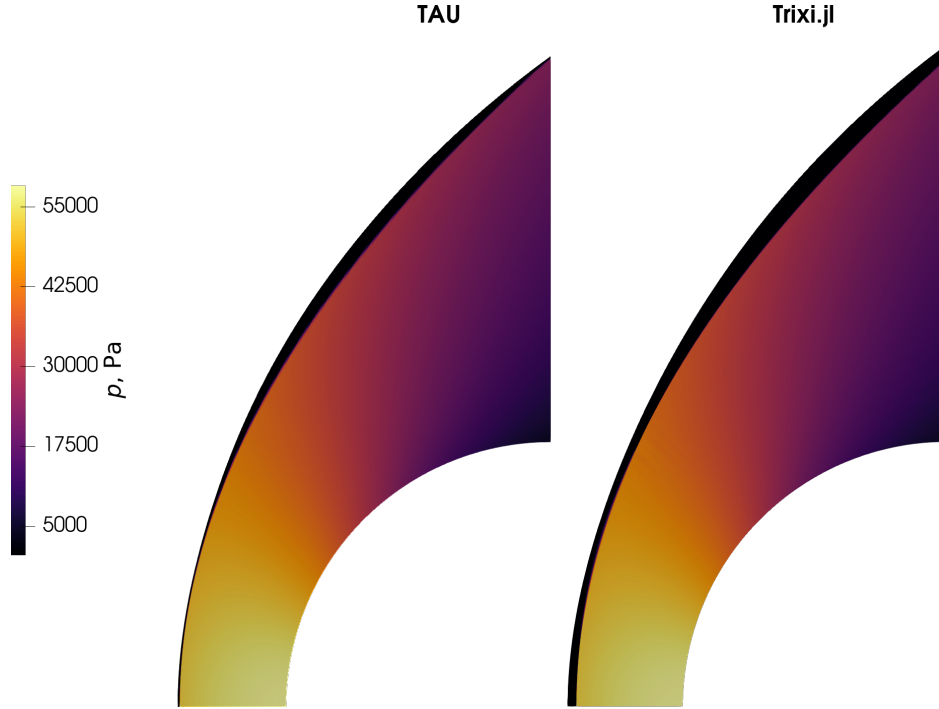


Figure 9: Flow-field pressure computed using the TAU code (left) and the developed entropy-conservative approach implemented in Trixi.jl (right) for the case of a constant specific heat ($\gamma = 1.4$).

Figure 9 shows the computed flow-field pressure for TAU and Trixi.jl simulations grid, with the Trixi.jl results computed using 2-nd order polynomials. Excellent agreement can be observed between the solvers. Since the Trixi.jl solution used a grid with several larger cells in the pre-shock region, the visualized results differ somewhat due to the different domains. For a more quantitative comparison, we evaluate the flow properties along the stagnation line.

Figure 10 shows the pressure and temperature along the stagnation line (the surface of the cylinder is located at $x = -4.5$ cm) computed using TAU and Trixi.jl, with the Trixi.jl simulation using 2-nd order polynomials. Excellent agreement can be seen between the solvers, thus confirming the validity of the basic solver components.

Now we consider the cases with temperature-dependent specific heats. Figure 11 shows the computed flow-field pressure for the case of the vibrational spectrum modelled by an infinite harmonic oscillator. Excellent qualitative

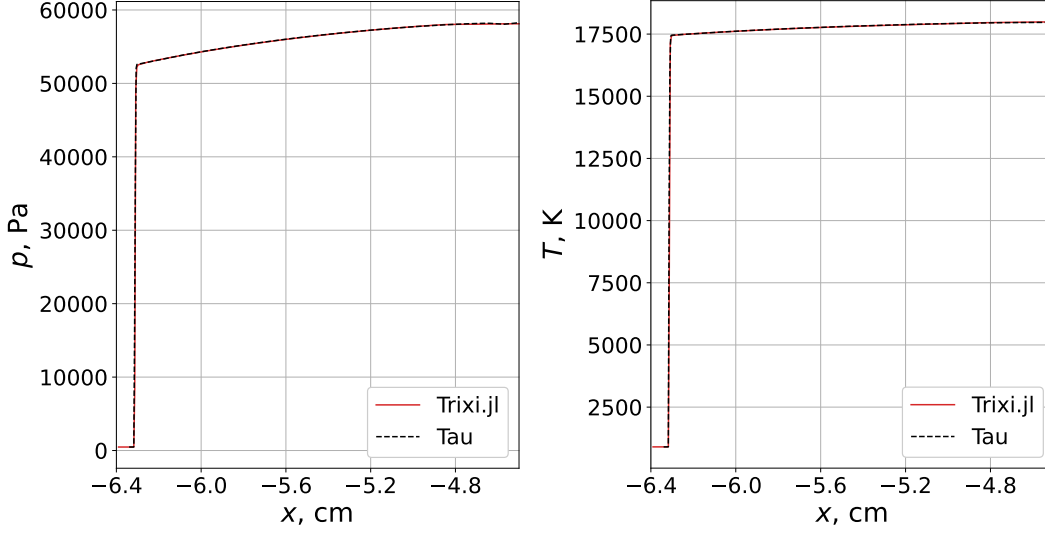


Figure 10: Pressure (left) and temperature (right) along the stagnation line for the case of $\gamma = 1.4$.

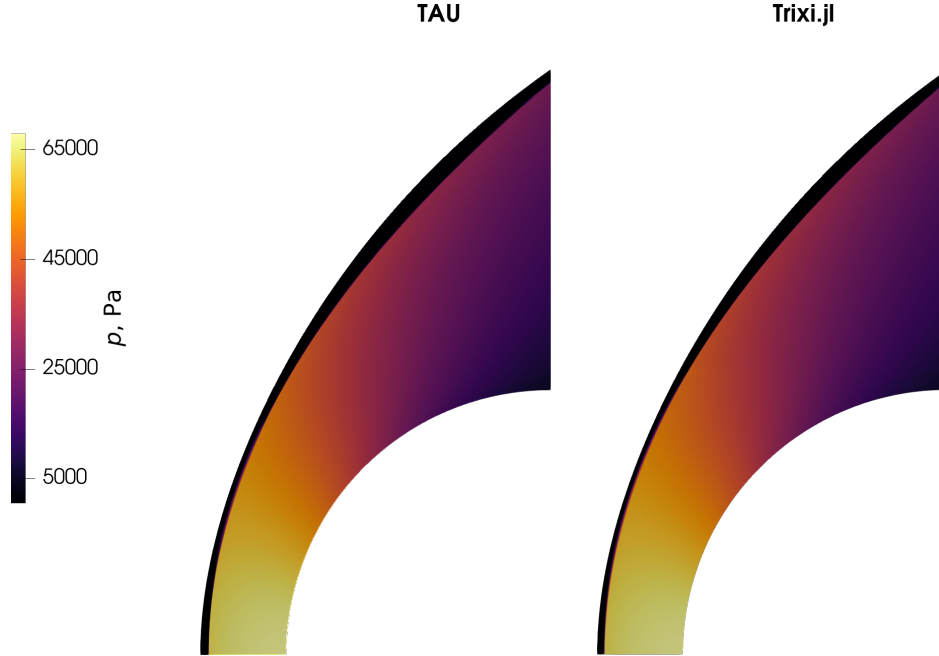


Figure 11: Flow-field pressure computed using the TAU code (left) and the developed entropy-conservative approach implemented in Trixi.jl (right) for the case of the infinite harmonic oscillator.

agreement can be seen between the simulations: even the smeared pressure jump region near the shock (where the shock is strong and not well-aligned with grid) is reproduced by the Trixi.jl implementation.

For a more detailed analysis, we look at the flow-field properties along the stagnation line $y = 0$ (assuming that the center of the cylinder is located at $(0, 0)$). Figure 12 shows the pressure and temperature along the stagnation line (the surface of the cylinder is located at $x = -4.5$ cm) computed using TAU and Trixi.jl for the two different vibrational spectrum models, i.e. infinite harmonic oscillator and the cut-off anharmonic oscillator, with the cut-off determined by the vibrational level where the vibrational energy starts decreasing with increasing level number. The Trixi.jl simulation used 3-rd order polynomials. We see good agreement between the solutions, although the Trixi.jl simulation exhibits a slightly higher post-shock temperature and a larger shock stand-off distance in the case of the infinite harmonic oscillator, and a lower post-shock temperature and smaller stand-off distance in the case of the cut-off

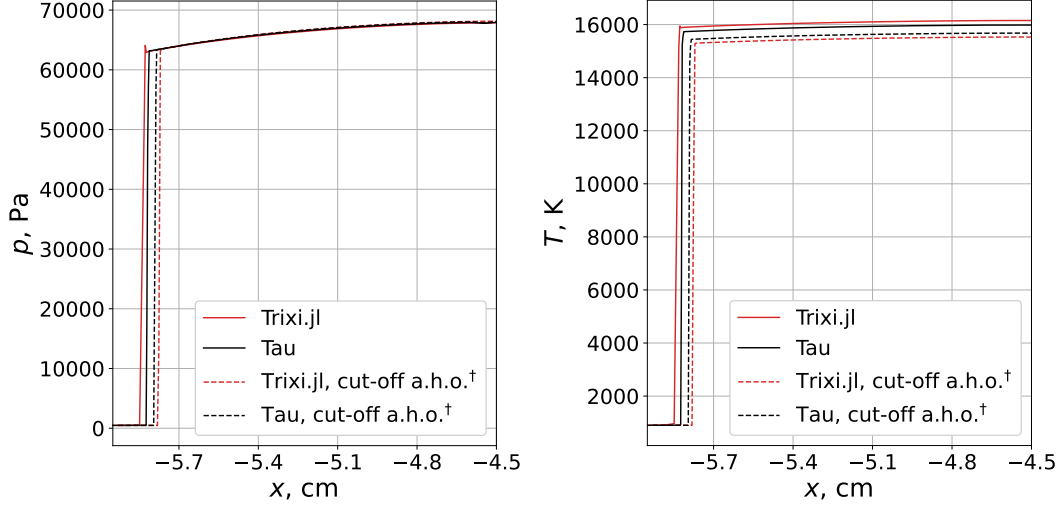


Figure 12: Pressure (left) and temperature (right) along the stagnation line for two different vibrational spectra models.

anharmonic oscillator. To investigate the source of the discrepancy, during the TAU simulations, the computed ratio of specific heats γ was output along with the other flow quantities. We then can plot it as a function of temperature in the corresponding cell, allowing to investigate the temperature dependence of γ .

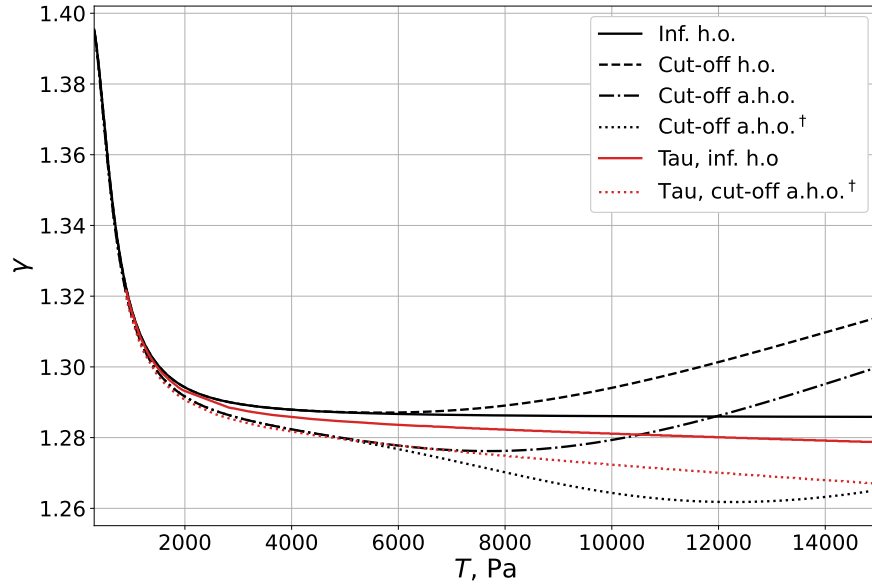


Figure 13: The heat capacity ratio γ for molecular oxygen as a function of temperature computed using TAU (red lines) and the various models considered in the present work (black lines).

Figure 13 shows the heat capacity ratio of molecular oxygen computed using TAU as a function of temperature for two models for the vibrational spectrum: the infinite harmonic oscillator and the cut-off anharmonic oscillator. It also shows the values of γ computed using the different vibrational spectra models used in the present work, already shown on Fig. 1. It can be seen that for the infinite harmonic oscillator model the TAU simulations had lower values of γ than the implementation in the present work, especially at higher temperatures, which explains the smaller stand-off distance computed using the TAU code [42]. Conversely, for the cut-off anharmonic oscillator model the results produced by TAU had higher values of γ in most of the considered temperature range, leading to a larger stand-off distance. Therefore, it can be concluded that the differences observed in the flow-field are due to differences in the implementation of thermodynamic gas properties.

Finally, we analyse the flow quantities in the expansion region, namely, along the outflow boundary given by $x = 0$. As the temperatures are lower in that region, and the shock is significantly weaker, the impact of discrepancies in the thermodynamical properties is expected to be less significant. Slightly more differences were observed between Trixi.jl simulations using different grid and polynomial orders in this region, therefore, more results are presented: simulations were carried out for 2-nd, 3-rd, and 4-th order polynomials on 30×30 and 60×60 grids.

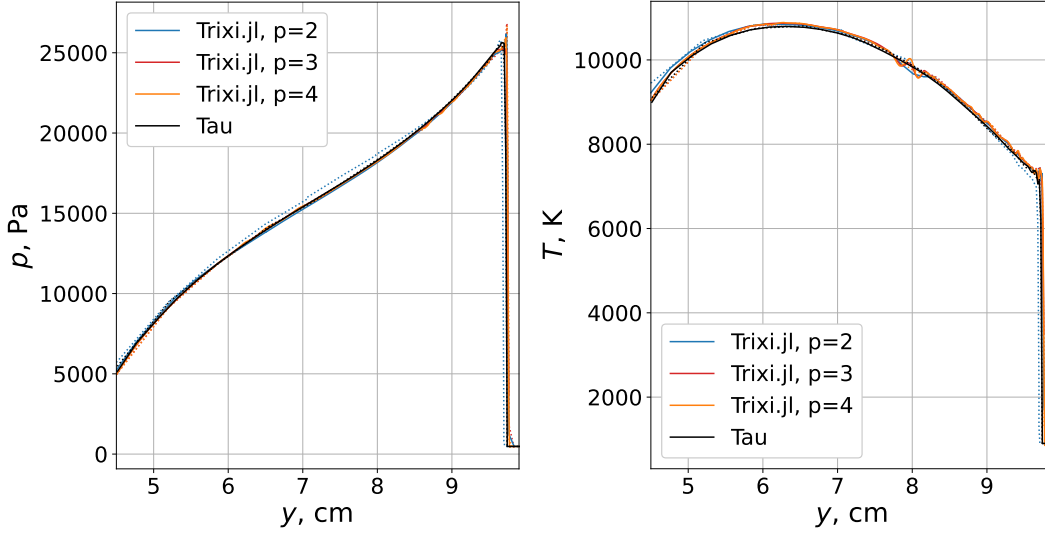


Figure 14: Pressure (left) and temperature (right) along the outflow boundary, infinite harmonic oscillator model. Solid lines correspond denote simulations conducted on a 60×60 grid, dotted lines denote simulations conducted on a 30×30 grid.

Figure 14 shows the pressure and temperature in the expansion region along the line $x = 0$ (the surface of the cylinder is located at $y = 4.5$ cm) for the infinite harmonic oscillator model of the vibrational spectrum. Solid lines correspond to the 60×60 grid, dotted lines correspond to the 30×30 grid. We see that all simulation results agree very well, with only the 2-nd order DG simulation on the coarse 30×30 grid deviating slightly in terms of pressure. The Trixi.jl-based DG simulations predict a sharper shock, but use of the higher-order polynomials also leads to the presence of irregularities (seen on the temperature profile at $y = 8$ cm).

Finally, Fig. 15 shows the pressure and temperature along the line $x = 0$ for the cut-off anharmonic oscillator model. Similarly to the infinite harmonic oscillator case, only the DG simulation using 2-nd order polynomials on a 30×30 grid displays any noticeable discrepancy in terms of the pressure from the other results. The higher-order simulations also exhibit slight oscillations in the temperature; however, they were not found to affect the stability of the simulations in general.

Therefore, it can be concluded that the developed approach for entropy-stable simulations of high-enthalpy flows of gases with internal degrees of freedom provides accurate results, and has good properties in terms of computational performance.

5 Conclusion

An approach to the computation of entropy-conserving fluxes for gases with arbitrary internal energies has been developed, based on the approximation of entropy via a numerical quadrature and subsequent application of the mean value theorem to express the jumps in entropy via jumps in the temperature. For a calorically perfect gas, the fluxes have been shown to reduce to well-known expressions available in literature. A significant advantage of the proposed approach is its independence on the exact expressions for the internal energy, as they are only required in the pre-computation step, and the flow simulations only perform linear interpolation, the cost of which is independent on the exact form of the internal energy.

The flux function has been implemented in the Trixi.jl framework and simulations of a Mach 10.5 flow over a cylinder were performed for three different internal energy functions. Comparisons with computations carried out using the DLR TAU solver show very good agreement in the flow-field quantities; with some discrepancies that can be attributed to a mismatch between the thermodynamical data used in the TAU solver and that used in the present work.

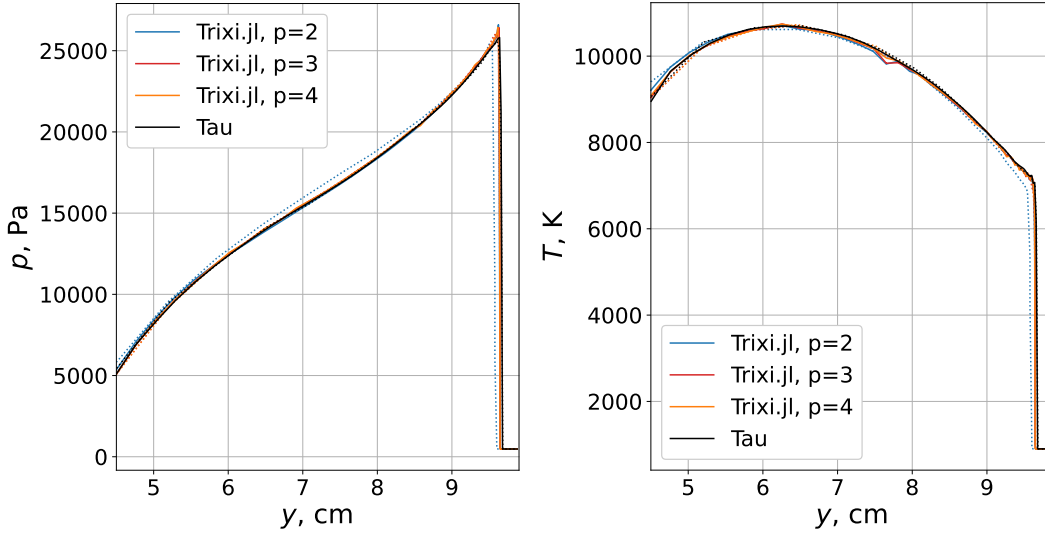


Figure 15: Pressure (left) and temperature (right) along the outflow boundary, cut-off anharmonic oscillator model. Solid lines correspond denote simulations conducted on a 60×60 grid, dotted lines denote simulations conducted on a 30×30 grid.

Further future extensions of the work include the generalization of the scheme to multi-species reacting flows, and its application to viscous flows.

Acknowledgments

This work has been supported by the German Research Foundation within the research unit DFG-FOR5409. Georgii Oblapenko also acknowledges the support of the Humboldt Foundation for his guest research stay at the German Aerospace Center (DLR) Institute of Aerodynamics and Flow Technology in Göttingen, during which the results with the DLR TAU solver had been obtained.

References

- [1] Y. BAI AND K. J. FIDKOWSKI, *Continuous artificial-viscosity shock capturing for hybrid Discontinuous Galerkin on adapted meshes*, AIAA J., 60 (2022), pp. 5678–5691, <https://doi.org/10.2514/1.J061783>.
- [2] F. BASILE, J.-B. CHAPELIER, M. DE LA LLAVE PLATA, R. LARAUFIE, AND P. FREY, *Unstructured h-and hp-adaptive strategies for discontinuous Galerkin methods based on a posteriori error estimation for compressible flows*, Comput. Fluids, 233 (2022), p. 105245, <https://doi.org/j.compfluid.2021.105245>.
- [3] M. BOHM, S. SCHERMENG, A. R. WINTERS, G. J. GASSNER, AND G. B. JACOBS, *Multi-element SIAC filter for shock capturing applied to high-order discontinuous Galerkin spectral element methods*, J. Sci. Comput., 81 (2019), pp. 820–844, <https://doi.org/10.1007/s10915-019-01036-8>.
- [4] G. V. CANDLER AND R. W. MACCORMACK, *Computation of weakly ionized hypersonic flows in thermochemical nonequilibrium*, J. Thermophys. Heat Transfer, 5 (1991), pp. 266–273, <https://doi.org/10.2514/3.260>, <https://arc.aiaa.org/doi/10.2514/3.260> (accessed 2021-04-06).
- [5] M. CAPITELLI, G. COLONNA, L. MARRAFFA, D. GIORDANO, D. GIORDANO, AND B. WARMBEIN, *Tables of internal partition functions and thermodynamic properties of high-temperature Mars-atmosphere species from 50K to 50000K*, no. STR-246, 2005.
- [6] J. CHAN, *On discretely entropy conservative and entropy stable discontinuous Galerkin methods*, J. Comput. Phys., 362 (2018), pp. 346–374, <https://doi.org/10.1016/j.jcp.2018.02.033>.
- [7] P. CHANDRASHEKAR, *Kinetic energy preserving and entropy stable finite volume schemes for compressible Euler and Navier-Stokes equations*, Commun. Comput. Phys., 14 (2013), pp. 1252–1286, <https://doi.org/10.4208/cicp.170712.010313a>.

- [8] E. J. CHING, Y. LV, P. GNOFFO, M. BARNHARDT, AND M. IHME, *Shock capturing for discontinuous Galerkin methods with application to predicting heat transfer in hypersonic flows*, J. Comput. Phys., 376 (2019), pp. 54–75, <https://doi.org/10.1016/j.jcp.2018.09.016>.
- [9] A. F. CORTESI, P. G. CONSTANTINE, T. E. MAGIN, AND P. M. CONGEDO, *Forward and backward uncertainty quantification with active subspaces: application to hypersonic flows around a cylinder*, J. Comput. Phys., 407 (2020), p. 109079, <https://doi.org/10.1016/j.jcp.2019.109079>.
- [10] A. FOG, *Instruction tables: List of instruction latencies, throughputs and micro-operation breakdowns for Intel, AMD and VIA CPUs*, URL http://www.agner.org/optimize/instruction_tables.pdf, (2020).
- [11] L. FRIEDRICH, A. R. WINTERS, D. C. DEL REY FERNÁNDEZ, G. J. GASSNER, M. PARSANI, AND M. H. CARPENTER, *An entropy stable h/p non-conforming discontinuous Galerkin method with the summation-by-parts property*, J. Sci. Comput., 77 (2018), pp. 689–725, <https://doi.org/10.1007/s10915-018-0733-7>.
- [12] G. J. GASSNER AND A. R. WINTERS, *A novel robust strategy for discontinuous Galerkin methods in computational fluid mechanics: Why? When? What? Where?*, Front. Phys., 8 (2021), p. 500690, <https://doi.org/10.3389/fphy.2020.500690>.
- [13] A. GOUASMI, K. DURAISAMY, AND S. M. MURMAN, *Formulation of entropy-stable schemes for the multicomponent compressible Euler equations*, Comput. Methods Appl. Mech. Eng., 363 (2020), p. 112912, <https://doi.org/10.1016/j.cma.2020.112912>.
- [14] K. HANNEMANN, J. M. SCHRAMM, A. WAGNER, S. KARL, AND V. HANNEMANN, *A closely coupled experimental and numerical approach for hypersonic and high enthalpy flow investigations utilising the HEG shock tunnel and the DLR TAU code*, Tech. Report RTO-EN-AVT-186, VKI, 2010.
- [15] A. HARTEN, P. D. LAX, C. D. LEVERMORE, AND W. J. MOROKOFF, *Convex entropies and hyperbolicity for general Euler equations*, SIAM journal on numerical analysis, 35 (1998), pp. 2117–2127, <https://doi.org/10.1137/S0036142997316700>.
- [16] S. HENNEMANN, A. M. RUEDA-RAMÍREZ, F. J. HINDENLANG, AND G. J. GASSNER, *A provably entropy stable subcell shock capturing approach for high order split form DG for the compressible Euler equations*, J. Comput. Phys., 426 (2021), p. 109935, <https://doi.org/10.1016/j.jcp.2020.109935>.
- [17] D. S. HOSKIN, R. L. VAN HEYNINGEN, N. C. NGUYEN, J. VILA-PÉREZ, W. L. HARRIS, AND J. PERAIRE, *Discontinuous Galerkin methods for hypersonic flows*, arXiv preprint arXiv:2312.17619, (2023), <https://doi.org/10.48550/arXiv.2312.17619>.
- [18] F. ISMAIL AND P. L. ROE, *Affordable, entropy-consistent Euler flux functions II: Entropy production at shocks*, J. Comput. Phys., 228 (2009), pp. 5410–5436, <https://doi.org/10.1016/j.jcp.2009.04.021>.
- [19] A. JAMESON, *Formulation of kinetic energy preserving conservative schemes for gas dynamics and direct numerical simulation of one-dimensional viscous compressible flow in a shock tube using entropy and kinetic energy preserving schemes*, J. Sci. Comput., 34 (2008), pp. 188–208, <https://doi.org/10.1007/s10915-007-9172-6>.
- [20] R. F. JOHNSON AND A. D. KERCHER, *A conservative discontinuous Galerkin discretization for the chemically reacting Navier-Stokes equations*, J. Comput. Phys., 423 (2020), p. 109826, <https://doi.org/10.1016/j.jcp.2020.109826>.
- [21] S. KARL AND T. BYKERK, *Sustainable space technologies—strategies toward a predictive aerothermal design of re-useable space transportation systems*, Rev. Sci. Instrum., 95 (2024), <https://doi.org/10.1063/5.0177075>.
- [22] S. KARL, J. MARTINEZ SCHRAMM, AND K. HANNEMANN, *High enthalpy cylinder flow in HEG: A basis for CFD validation*, in 33rd AIAA Fluid Dynamics Conference and Exhibit, 2003, p. 4252, <https://doi.org/10.2514/6.2003-4252>.
- [23] M. KRONBICHLER, *High-performance implementation of discontinuous Galerkin methods with application in fluid flow*, in Efficient High-Order Discretizations for Computational Fluid Dynamics, M. Kronbichler and P.-O. Persson, eds., Springer, Cham, 2021, pp. 57–115, https://doi.org/10.1007/978-3-030-60610-7_2.
- [24] J. KUSCH, R. G. MCCLARREN, AND M. FRANK, *Filtered stochastic Galerkin methods for hyperbolic equations*, J. Comput. Phys., 403 (2020), p. 109073.
- [25] E. KUSTOVA, M. MEKHONOSHINA, AND G. OBLAPENKO, *On the applicability of simplified state-to-state models of transport coefficients*, Chem. Phys. Lett., 686 (2017), pp. 161–166, <https://doi.org/10.1016/j.cplett.2017.08.041>.

- [26] Y. LIN AND J. CHAN, *High order entropy stable discontinuous Galerkin spectral element methods through subcell limiting*, J. Comput. Phys., 498 (2024), p. 112677, <https://doi.org/10.1016/j.jcp.2023.112677>.
- [27] M.-S. LIOU, *A sequel to AUSM: AUSM+*, J. Comput. Phys., 129 (1996), pp. 364–382, <https://doi.org/10.1006/jcph.1996.0256>.
- [28] A. MACK AND V. HANNEMANN, *Validation of the unstructured DLR-TAU-Code for hypersonic flows*, in 32nd AIAA Fluid dynamics conference and exhibit, 2002, p. 3111, <https://doi.org/10.2514/6.2002-3111>.
- [29] B. J. MCBRIDE, *NASA Glenn coefficients for calculating thermodynamic properties of individual species*, tech. report, National Aeronautics and Space Administration, John H. Glenn Research Center, 2002.
- [30] C. MICHOSKI, C. DAWSON, E. J. KUBATKO, D. WIRASAET, S. BRUS, AND J. J. WESTERINK, *A comparison of artificial viscosity, limiters, and filters, for high order discontinuous Galerkin solutions in nonlinear settings*, J. Sci. Comput., 66 (2016), pp. 406–434, <https://doi.org/10.1007/s10915-015-0027-2>.
- [31] P. MOSSIER, A. BECK, AND C.-D. MUNZ, *A p-adaptive discontinuous Galerkin method with hp-shock capturing*, J. Sci. Comput., 91 (2022), p. 4, <https://doi.org/10.1007/s10915-022-01770-6>.
- [32] E. NAGNIBEDA AND E. KUSTOVA, *Non-equilibrium reacting gas flows: kinetic theory of transport and relaxation processes*, Springer Science & Business Media, Heidelberg, 2009, <https://doi.org/10.1007/978-3-642-01390-4>.
- [33] G. OBLAPENKO AND M. TORRILHON, *Reproducibility repository for "entropy-conservative high-order methods for high-enthalpy gas flows"*. https://github.com/knstmr/paper-ec_trixi_inte, 2024, <https://doi.org/10.5281/zenodo.10869717>.
- [34] A. PEYVAN, K. SHUKLA, J. CHAN, AND G. KARNIADAKIS, *High-order methods for hypersonic flows with strong shocks and real chemistry*, J. Comput. Phys., (2023), p. 112310, <https://doi.org/10.1016/j.jcp.2023.112310>.
- [35] C. RACKAUCKAS AND Q. NIE, *Differentialequations.jl—a performant and feature-rich ecosystem for solving differential equations in Julia*, J. Open Res. Softw., 5 (2017), <https://doi.org/10.5334/jors.151>.
- [36] H. RANOCHA, *Comparison of some entropy conservative numerical fluxes for the Euler equations*, J. Sci. Comput., 76 (2018), pp. 216–242, <https://doi.org/10.1007/s10915-017-0618-1>.
- [37] H. RANOCHA, M. SCHLOTTKE-LAKEMPER, J. CHAN, A. M. RUEDA-RAMÍREZ, A. R. WINTERS, F. HINDENLANG, AND G. J. GASSNER, *Efficient implementation of modern entropy stable and kinetic energy preserving discontinuous Galerkin methods for conservation laws*, ACM Trans. Math. Softw., 49 (2023), pp. 1–30, <https://doi.org/10.1145/3625559>.
- [38] H. RANOCHA, M. SCHLOTTKE-LAKEMPER, A. R. WINTERS, E. FAULHABER, J. CHAN, AND G. J. GASSNER, *Adaptive numerical simulations with Trixi.jl: A case study of Julia for scientific computing*, arXiv preprint arXiv:2108.06476, (2021), <https://doi.org/10.21105/jcon.00077>.
- [39] F. RENAC, *Entropy stable, robust and high-order DGSEM for the compressible multicomponent Euler equations*, J. Comput. Phys., 445 (2021), p. 110584, <https://doi.org/10.1016/j.jcp.2021.110584>.
- [40] M. SCHLOTTKE-LAKEMPER, G. J. GASSNER, H. RANOCHA, AND A. R. WINTERS, *Trixi.jl: Adaptive high-order numerical simulations of hyperbolic PDEs in Julia*. <https://github.com/trixi-framework/Trixi.jl>, 08 2020, <https://doi.org/10.5281/zenodo.3996439>.
- [41] J. B. SCOGGINS, V. LEROY, G. BELLAS-CHATZIGEORGIS, B. DIAS, AND T. E. MAGIN, *Mutation++: Multi-component thermodynamic and transport properties for ionized gases in C++*, SoftwareX, 12 (2020), p. 100575, <https://doi.org/10.1016/j.softx.2020.100575>.
- [42] J. SINCLAIR AND X. CUI, *A theoretical approximation of the shock standoff distance for supersonic flows around a circular cylinder*, Phys. Fluids, 29 (2017), <https://doi.org/10.1063/1.4975983>.
- [43] R. C. SMITH, *Uncertainty quantification: theory, implementation, and applications*, SIAM, Philadelphia, PA, 2013, <https://doi.org/10.5555/2568154>.
- [44] E. TADMOR, *Entropy stability theory for difference approximations of nonlinear conservation laws and related time-dependent problems*, Acta Numer., 12 (2003), pp. 451–512, <https://doi.org/10.1017/S0962492902000156>.
- [45] Z. WANG, K. FIDKOWSKI, R. ABGRALL, F. BASSI, D. CARAENI, A. CARY, H. DECONINCK, R. HARTMANN, K. HILLEWAERT, H. HUYNH, N. KROLL, G. MAY, P.-O. PERSSON, B. VAN LEER, AND M. VISBAL, *High-order CFD methods: current status and perspective*, Int. J. Numer. Meth. Fluids, 72 (2013), pp. 811–845, <https://doi.org/10.1002/flid.3767>.

- [46] X. ZHANG AND C.-W. SHU, *Maximum-principle-satisfying and positivity-preserving high-order schemes for conservation laws: survey and new developments*, Proc. R. Soc. A, 467 (2011), pp. 2752–2776, <https://doi.org/10.1098/rspa.2011.0153>.